

Resonance-type bimorph-based high-speed atomic force microscopy: real-time imaging and distortion correction

Wei Cai^{1,2}, Jianyong Zhao², Weitao Gong¹, Haiyun Fan¹ and Guangyi Shang^{1,2}

¹ Department of Applied Physics, Beihang University, Beijing 100191, People's Republic of China

² Key laboratory of Micro-nano Measurement-Manipulation and Physics (Ministry of Education), Beihang University, Beijing 100191, People's Republic of China

E-mail: gyshang@buaa.edu.cn

Received 26 August 2014, revised 30 September 2014

Accepted for publication 8 October 2014

Published 7 November 2014

Abstract

Resonance-type bimorph-based high-speed atomic force microscopy (HSAFM) capable of operating in the sample-scan and tip-scan modes is presented in this paper. The working principle of the high-speed scanner, the experimental setup, and the data collection system are described in detail. The main characteristic of the high-speed scanner is the use of a piezoelectric bimorph, where one of the piezoelectric layers is used to drive the bimorph beam to scan at a high speed and the other monitors the bimorph vibration. Image distortions due to the phase-lag and sinusoidal scanning are analyzed and simulated. The correction methods for the compensation of the phase-lag and nonlinear movement are proposed based on data shift and nonlinear mapping relations, respectively. The HSAFM imaging at the maximum rate of ~30 frames per second is demonstrated with our data collection and correction program. The image distortions caused by the phase-lag and sinusoidal scanning are effectively eliminated in real-time. This work would provide useful methods for the development of HSAFM and applications in the observation of dynamic processes at nanoscale.

Keywords: atomic force microscopy, high-speed atomic force microscopy, bimorph-based scanner, image distortion correction

 Online supplementary data available from stacks.iop.org/MST/25/125404

(Some figures may appear in colour only in the online journal)

1. Introduction

As a promising tool for the study of dynamic processes at nanoscale, the high-speed atomic force microscope (HSAFM) has attracted considerable attention during the last decade [1, 2]. HSAFM expands applications of conventional AFM to various fields such as *in-situ* observation of dynamic biological events [3–6], mapping structure changing processes under an external field [7, 8], real-time manipulation of nano-objects [9], and high-speed lithography [10, 11]. In order to perform the experiments above, many different approaches for fast scanning have been proposed and developed that could be divided

into two categories: (i) increase the resonance frequency of the conventional scanners; and (ii) scan at the increased resonance frequency of those. The former is designed based on the combination of piezoelectric stack actuators and a flex mechanism with a resonance frequency much higher than those of conventional scanners [12, 13]. The latter is fabricated by using a small mechanical oscillator, such as a tuning fork [14–16], a brass bar [17], a quartz bar [18], or a bimorph beam [19, 20]. The notable advantages of the resonance-type scanners include: (i) a simple structure which is easy to fabricate, since a complicated flexible structure is not needed; (ii) a large scan range; and (iii) a low drive voltage with a sinusoidal waveform, where high-voltage

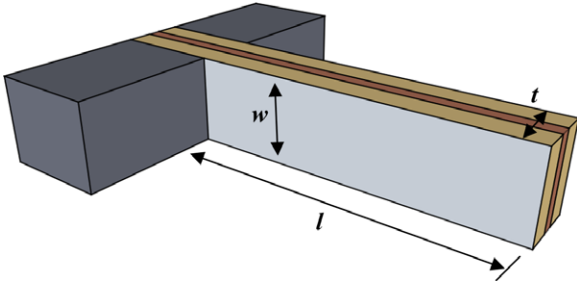


Figure 1. Schematic of the resonance-type bimorph-based scanner for HSAFM.

amplifiers are not needed. Besides, the scanner driven by a sinusoidal waveform can help eliminate harmonic excitation of the scanner resonance modes [21]. Therefore, the resonance-type fast scanners have been widely used in HSAFM.

The resonance-type bimorph-based fast scanner for HSAFM has been successfully developed in our laboratory, which can work in sample-scan and tip-scan modes [19, 20]. The main characteristic of the scanner is the use of a piezoelectric bimorph, where one of the piezoelectric layers is used to drive the bimorph beam to scan in a high speed and the other monitors the beam vibration. The significant advantage of the bimorph-based scanner with respect to the tuning fork is the fact that the imaging rate and the maximum scan range can be adjusted by changing the bimorph beam length, providing an easy method for the observation of samples with different properties. Furthermore, compared with the brass and quartz bar scanners, the bimorph-based scanner has the ability to detect the vibration of itself including amplitude and phase, which provides useful information for correcting image distortion.

Since sinusoidal scanning is used in resonance-type scanners, the scanning speed varies as a sinusoidal waveform, resulting in the tip/sample's velocity being slow at both ends and fast at the middle part of each scan line. However, the sample time between point and point is usually the same, leading to redundant sample points in both left and right parts of the image and fewer sample points in the middle area. In this case, the image composed of the sampling points is distorted [22–24]. In addition, we also found that image distortion can be caused by the phase-lag between the scan drive voltage and the movement of the scanner. Therefore, it is important to conduct real-time distortion correction while performing high-speed imaging. Unfortunately, little work on the phase-lag induced distortion correction has been reported up to now.

In this paper, we focus on the high-speed imaging and distortion correcting methods. The HSAFM experimental setup, including the resonance-type bimorph-based scanner, hardware configuration, and data collection system, is first presented in detail. Image distortions due to the phase-lag and sinusoidal scanning are then analyzed and simulated. The image distortion caused by the phase-lag is compensated by applying a data shift method on the collected data, and the distortion introduced by nonlinear movement is corrected by using nonlinear mapping relations. High-speed imaging at the maximum rate of ~30 frames per second (FPS) is demonstrated. The image distortions caused by the phase-lag and sinusoidal scanning are

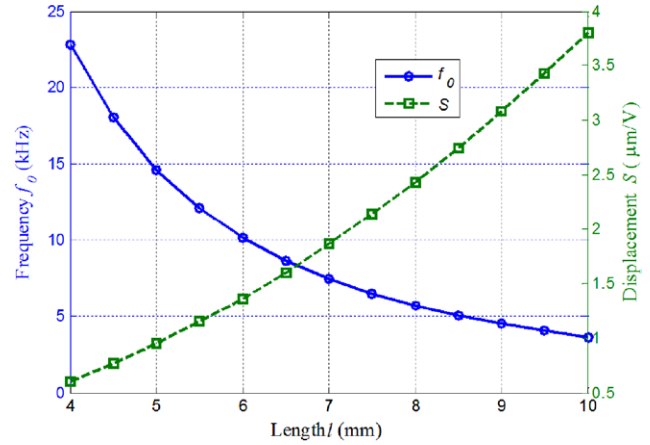


Figure 2. The relationship curves between the resonance frequency (the line scan rate)/displacement sensitivity and the beam length, calculated with parameters of width $w = 1.5$ mm, thickness $t = 0.8$ mm, $h = 0.3$ mm, elastic modulus $E = 5.2 \times 10^{10} \text{ N m}^{-2}$, the density $\rho = 6.5 \times 10^3 \text{ kg m}^{-3}$, and the piezoelectric coefficient $d_{31} = 1.71 \times 10^{-10} \text{ m V}^{-1}$. The Q -factors were measured to be about 20.

effectively eliminated in real-time. This work would provide useful methods for the development of HSAFM and applications in the observation of dynamic processes at nanoscale.

2. Experimental setup

2.1. Resonance-type bimorph-based scanner

The resonance-type bimorph-based scanner for HSAFM is schematically shown in figure 1. By means of the specially designed holders, the bimorph consisting of two piezoelectric layers attached to a conductive middle shim is rigidly clamped at one of its ends, forming a cantilevered beam with dimensions of length l , width w , and thickness t . A small sample stage or an AFM tip could be fixed on the free end of the beam for operating in the sample-scan mode or tip-scan mode, respectively.

For high-speed imaging, two important parameters have to be taken into account, including the resonance frequency f_0 and the displacement sensitivity S of the free end of the beam, where the unit of f_0 is kHz and that of S is $\mu\text{m/V}$. Obviously, the resonance frequency corresponds to the line scan rate of the scanner and the displacement sensitivity is related to the scan range. Based on the theory for an homogeneous beam with a uniform cross section, f_0 and S can be estimated by the following equations [19]:

$$f_0 = (\eta_0^2 / 2\pi) (t / l^2) (E / 12\rho)^{1/2} \quad (1)$$

$$S = d_{31}(l / h)^2 Q. \quad (2)$$

Here, E is the Young's modulus, $\eta_0 = 1.875$, ρ is the mass density, Q is the quality factor of the beam that is defined as $f_0/\Delta f$ and Δf is the full width at half maximum, h is the thickness of one piezoelectric layer, d_{31} is the relevant piezoelectric coefficient. From the above equations, it is easy to find that the imaging rate can be adjusted by changing the beam length, and the scan range can also be done by changing the beam length or the drive voltage. The relationship curves between f_0 or S and the beam length l were calculated and given in figure 2.

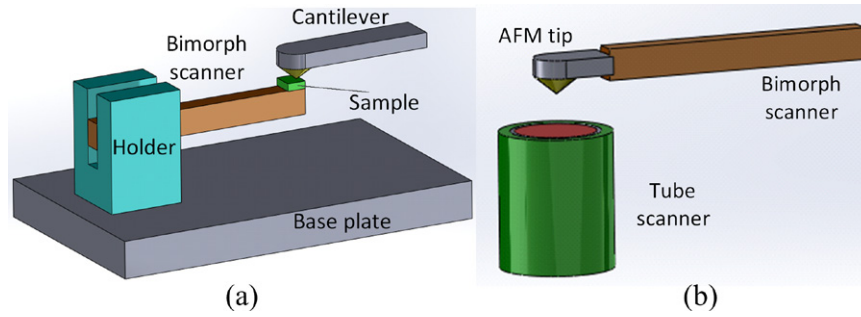


Figure 3. Schematics of the resonance-type bimorph-based scanner, operating in (a) the sample-scan mode and (b) the tip-scan mode.

The other parameter related to high-speed imaging is FPS, which is given by

$$\text{FPS} = f_0 / N_L \quad (3)$$

where N_L is the number of lines in one frame. For example, if the line scan rate f_0 is set to 1.0 kHz and the number of lines is 100, HSAFM images can be taken at 10 FPS.

2.2. HSAFM setup

A home-made HSAFM system working in the contact-mode has been successfully built, in which a sample scan and tip scan can be employed, respectively. In the sample-scan mode, as shown in figure 3(a), the bimorph scanner is mounted on the top of a quartered single tube scanner (not shown in the figure). The longitudinal axis of the bimorph is carefully aligned with the y-direction of the tube scanner, forming a hybrid scan unit. High-speed scanning is realized with the bimorph beam vibrating near its resonance frequency, while slow scanning is performed by means of the tube scanner. The tube scanner can also provide motion in the z-direction for height control on a frame-by-frame timescale when HSAFM imaging [2, 25]. The mechanical properties of the micro cantilever beam are constructed to control the path of the tip over the surface of the sample [14]. In the tip-scan mode, an AFM cantilever is fixed on the free end of the bimorph by using a specially designed tip holder, as shown in figure 3(b). In this mode, both fast and slow scans are carried out in the same way as those in the sample-scan mode. However, the scan range is restricted within $\sim 10 \mu\text{m}$ due to tracking optics, and false bending effects need to be removed by subtracting the background signal in the program [20]. For HSAFM imaging, the laser beam deflection method is adopted to detect the motion of the AFM cantilever. The aspheric lens is used for focusing the collimated laser beam on a small cantilever. The commercially available cantilevers, Bio-Lever mini (BL-AC40TS-C2, Olympus) with the spring constant of 0.1 N m^{-1} and resonance frequency of 110 kHz, are used in the experiments.

2.3. Scan control and data collection

The control system consists of the conventional AFM controller, the high-speed scan, and data acquisition system. The conventional AFM controller includes the mechanism to approach the tip to the sample surface and the feedback circuits to keep an average height of the tip to the surface in the

z-axis during imaging. The high-speed system consists of the National Instruments data acquisition card (DAQ) (National Instruments, S-6115) and a homemade program for scan signal generation, real-time data acquisition, and image processing. One of the analog output (AO) channels of the DAQ card is connected to one of the piezo-layers of the bimorph for high-speed scanning in the x-axis, while the other AO channel is connected to the tube scanner for scanning in the y-axis by means of high-voltage amplifiers. The waveforms of the signals to drive the hybrid scan device are shown in figure 4. The induced voltage from the other piezo-layer of the bimorph is used as the sensing signal, which is amplified and fed to one of the analog input (AI) channels for monitoring the bimorph vibration, providing information about the oscillation amplitude and the phase difference between the driving signal and the sensing signal. The AFM deflection signal from the four-quadrant position sensitive detector (PSD) is fed to the other AI channel to create images. The synchronization of the scan voltage with the data acquisition is realized by the data collection system.

3. Analysis and simulation for image distortions

In order to carry out real-time imaging, image distortions due to the phase-lag and sinusoidal scanning are analyzed and simulated, as follows.

3.1. Image distortion caused by phase-lag

It is well-known that a topographic or deflection signal of a conventional AFM is synchronized with its scan drive voltage, usually forming an AFM image with small nonlinear distortion due to nonlinear movement of the piezoelectric scanner. This nonlinear distortion can be corrected by many existing methods [26]. In HSAFM, the imaging signals should be also synchronized with the scan drive voltage. However, it was found that the HSAFM imaging signals are highly asynchronous with the scan drive voltage, because a phase-lag $\varphi(\omega)$ exists between the drive voltage and the movement of the scanner, resulting in image distortion.

This phase-lag $\varphi(\omega)$ can be described by the dynamic equation (4) of a bimorph beam [27–29], where x is the displacement of the scanner, m is the effective mass of the vibrating system and γ is the damping constant. ω_0 is the resonance

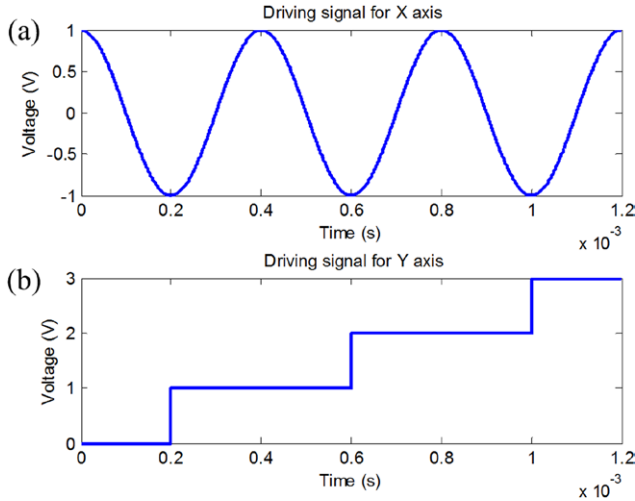


Figure 4. Waveforms of the scan voltages for the hybrid scanner: (a) for the x-axis a fast scan of the bimorph scanner; and (b) for the y-axis a slow scan of the tube scanner by means of high-voltage amplifiers.

frequency that can be expressed by $\omega_0 = \sqrt{k/m}$, k is the spring constant of the cantilever. $F_0 \cos \omega t$ is a periodic force which excites the scanner's motion.

$$\frac{d^2x}{dt^2} + \gamma \frac{dx}{dt} + \omega_0^2 x = \frac{F_0}{m} \cos \omega t \quad (4)$$

By introducing the Q factor such that $Q = \omega_0 / 2\gamma$ and solving equation (4), the displacement $x(t)$ can be deduced as

$$x(t) = x_0(\omega) \cos[\omega t - \varphi(\omega)] \quad (5)$$

where

$$x_0(\omega) = \frac{F_0 / k}{\sqrt{[1 - (\omega / \omega_0)^2]^2 + (\omega / \omega_0 Q)^2}} \quad (6)$$

and the frequency dependent phase-lag $\varphi(\omega)$ can be expressed by equation (7):

$$\tan \varphi(\omega) = \frac{1}{Q} \frac{\omega \omega_0}{\omega_0^2 - \omega^2}. \quad (7)$$

According to equations (4)–(7) and compared with the driving signal, the displacement or the sensing signal of the bimorph has a phase-lag $\varphi(\omega)$.

To demonstrate image distortion caused by the phase-lag, an image of a standard grating sample as given in figure 5(a) is simulated. The simulated results show that serious image distortion takes place due to the phase-lag, as shown in figure 5(b), which is very different from the nonlinear distortion. As mentioned above, the sensing signal from the bimorph scanner provides phase-lag information of the bimorph vibration and can be used for image correction. Figure 5(c) shows the relationship between the HSAFM collection/deflection signal (the solid line), the drive voltage (the dashed line), and the sensing signal (the dotted line), from which the phase-lag can be calculated, and in figure 5(c) it is $\sim 40^\circ$. It was found that if the HSAFM collection signal was

synchronized with the driving signal by means of the data collection system, the image phase-lag distortion could be effectively eliminated.

3.2. Image distortion due to sinusoidal scanning

To analyze the image distortion due to sinusoidal scanning, we assume that the phase-lag is zero and the displacement $x(t)$ of the bimorph scanner is expressed by

$$x(t) = -x_0 \cos(\omega t). \quad (8)$$

If each scan line consists of N pixels, the time period of scanning T , and the sampling rate t_s , the scanning time per line T can be estimated by

$$T = 2Nt_s. \quad (9)$$

The coefficient 2 means that in one period the tip or sample moves forward and then backward. So the angular frequency ω can be deduced as

$$\omega = 2\pi / T = \pi / Nt_s. \quad (10)$$

Substituting equation (10) into equation (8) yields

$$x = -x_0 \cos(\pi t / Nt_s) = -x_0 \cos(n\pi / N) \quad (11)$$

where t/t_s represents the pixel number n on each scan line.

Equation (11) gives the relationship between the displacement x and the pixel number n on each scan line. It is a cosine curve just like the drive voltage waveform. It is easy to see that the displacements are relatively smaller at both ends of each scan line because of n being close to 0 or N , and the sampling points are distributed intensively. In the middle part of each scan line, however, the displacements are larger and the sampling points are distributed sparsely since n is close to $N/2$. Thus, the image composed of the unevenly distributed sampling points is distorted along the scan axis.

As an example, the typical image distortion caused by sinusoidal scanning is shown in figure 6(a). The sample simulated here is also a standard grating as given in figure 5(a). It is evident that the center part of the image is compressed while two sides of the image are expanded. The difference between the linear and the sinusoidal scanning is shown in figure 6(b). For a linear scan, the relationship between the pixel number and the displacement is linear, as represented by the solid line. For a sinusoidal scan, the displacement is nonlinear to the pixel number as given by the dash line. That is the reason for the nonlinear image distortion.

4. Distortion correction methods

4.1. Phase-lag compensation

As we know, the phase-lag $\varphi(\omega)$ is frequency dependent. Once the line scan rate changes, the phase-lag value varies too. In order to compensate for the phase-lag, the phase difference between the scan drive signal and the sensing signal of the bimorph beam has to be measured before image correction. Based on the measured phase-lag value, the collected data can be shifted to the right point of each scan line.

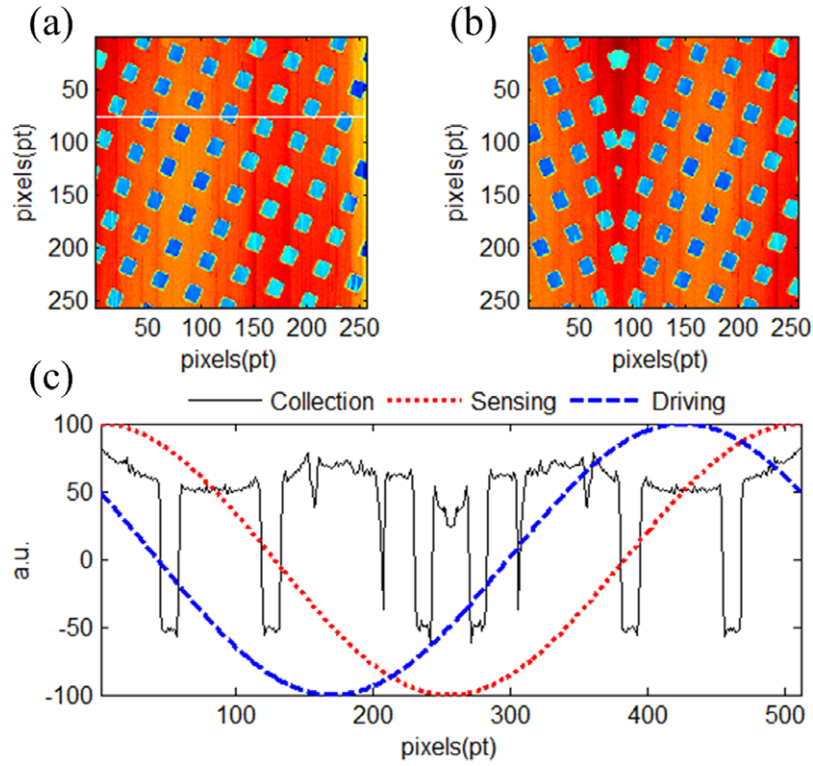


Figure 5. (a) The image of a standard grating sample. (b) The simulated image distortion caused by the phase-lag. (c) The relationship between the collection/deflection signal (solid line), the scan driving voltage (dash line), and sensing signal (dotted line) in HSAFM.

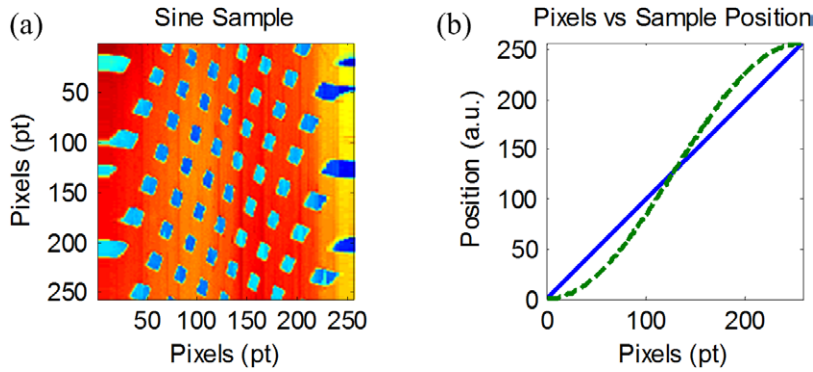


Figure 6. (a) The simulated image distortion caused by sinusoidal scanning. (b) The difference between the linear (solid line) and the sinusoidal scan (dash line).

Figure 7 gives the illustration of the compensation method for the correction of phase-lag induced distortion. Each dot in the figure represents a collected data point. The number of the data per one frame is $M \times 2N$. One frame consists of two images: scanned forward and backward. Generally, one of the forward or backward images with pixels $M \times N$ is displayed. While imaging, the collection system reads $2N$ data once per line in a fixed sampling rate, which is synchronized with the drive voltage. Because of the phase-lag, the starting point of the collection mismatches with the actual scan position. The key issue to compensate the phase-lag is to determine which point is the actual starting point in this line. That is, the number of data points that need to be shifted should be determined.

For example, as shown in figure 7, assume that the collected data per line starts from X_k rather than X_1 due to the phase-lag. The method of the compensation is to shift these data points before X_1 , and then to make X_1 the starting point of the line, because X_1 matches the actual scan position. Based on this idea, we put the first point X_k into the right end of the line and then move the following points one by one. Finally, the correct data structure for both forward (X_1 to X_N) and backward (X_N to X_1) data are built up. Obviously, a correct image can be formed by shifting the corresponding data line-by-line, since the number of collected data points per line (one cycle) is $2N$ and the measured phase-lag is θ degree. The value k can be estimated by the following relationship:

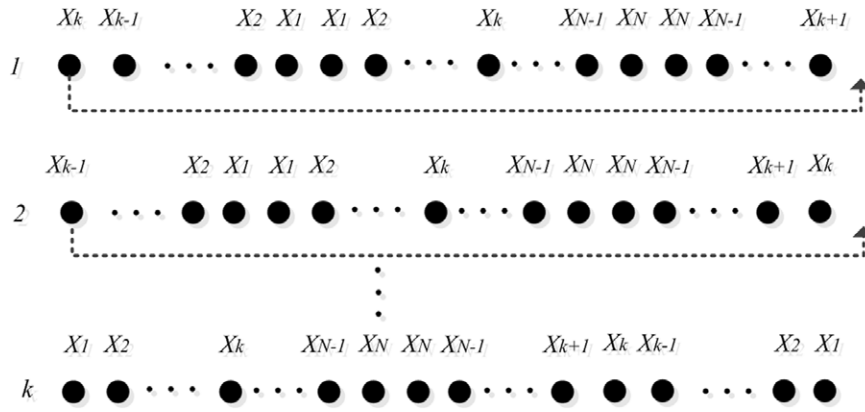


Figure 7. Illustration of the correction method to compensate phase-lag distortion.

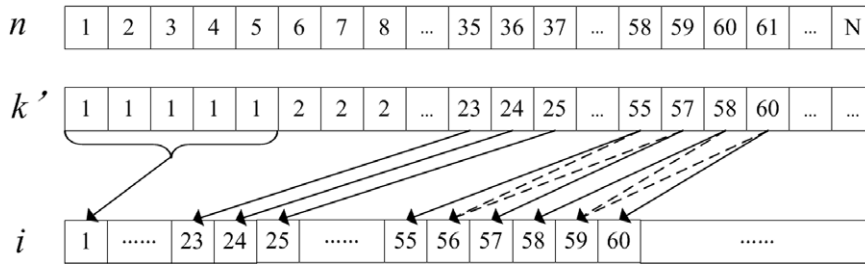


Figure 8. The corresponding mapping table k' between the pixel numbers in a nonlinear and linear scan. Line n represents a line from the distorted image (nonlinear) and line i represents the corrected line (linear).

$$\frac{k}{2N} = \frac{\theta}{360} \quad (12)$$

$$k = \theta N / 180. \quad (13)$$

Based on equation (13), it is easy to determine the value k since θ can be measured in our experiments.

which yields

$$k = \frac{1}{x_0} \left(x_n + \frac{1}{2} \right) + 1 \quad (17)$$

$$k = \frac{N-1}{2} \left[-\cos\left(\frac{n\pi}{N}\right) + 1 \right] + 1, n = 1, 2, 3, \dots, N. \quad (18)$$

4.2. Nonlinear correction for sinusoidal scanning

Because of the sinusoidal scanning, we need to put each data collected by the equal time intervals into the true spatial position. In other words, the collection system is linear but the displacement is nonlinear. The relationship between the linear and nonlinear scan can be deduced in the following way. The maximum scan range of the bimorph scanner is from $-L/2$ to $L/2$ and the number of the pixels in each line is N . If a linear scan is adopted, the displacement of one pixel is constant and can be expressed as

$$x_0 = L / (N - 1). \quad (14)$$

For a nonlinear scan, the displacement x_n can be expressed as follows:

$$x_n = -\frac{L}{2} \cos\left(\pi \frac{n}{N}\right), n = 1, 2, 3, \dots, N. \quad (15)$$

The method to correct such image distortion is to make the nonlinear displacement equal to a linear scan. So the following relationship should be satisfied:

$$-\frac{L}{2} + (k-1)x_0 = x_n \quad (16)$$

From equation (18), the values of k are not integers, and hence need to be rounded off. We use integer k' instead of k in the calculation. The following table can be used to correct the distorted image.

Figure 8 shows the relationships between the pixel numbers in a nonlinear and linear scan for $N = 128$ and the corresponding correction method. In this figure, line n represents a line from the distorted image and line i represents the corrected line. From the relationships k' it is easy to see that the distortions mainly concentrate on both left and right sides of the image due to the slow scan velocity. Since the scan velocity is close to that of the linear scan, the middle parts of the image often have less distortion. From the relationships in the illustration, it is clear to see that three mapping situations need to be addressed: the first situation is oversampling, the average value of the data at the first five pixels of the distorted line should be calculated and put in the first pixel of the corrected line. For the second one, the data at the distorted and corrected pixels have a one-to-one correspondence and no calculation is needed. The third case is undersampling; because there is

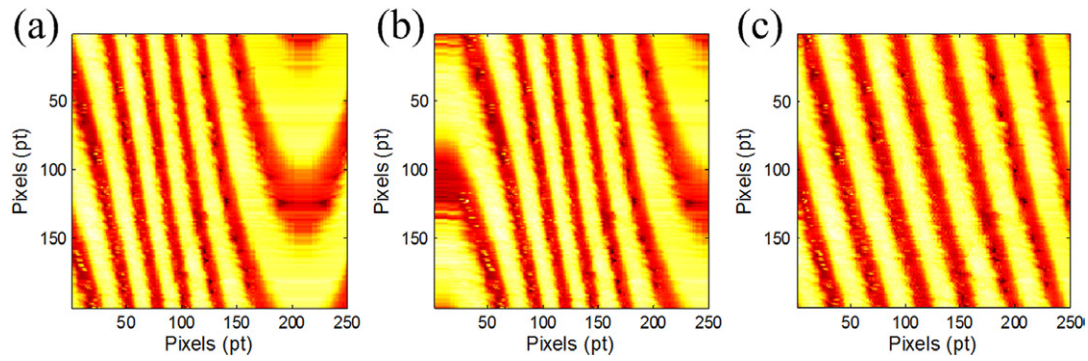


Figure 9. HSAFM images of a piece of the CD disc. (a) The original image; (b) the image after the phase-lag compensation image; and (c) the final image after nonlinear correction. The scan range is $\sim 10\mu\text{m}$ and the imaging rate is ~ 15 FPS. The movie is shown in the supplementary data as movie1.gif (stacks.iop.org/MST/25/125404). During imaging the sample position was manually adjusted slightly.

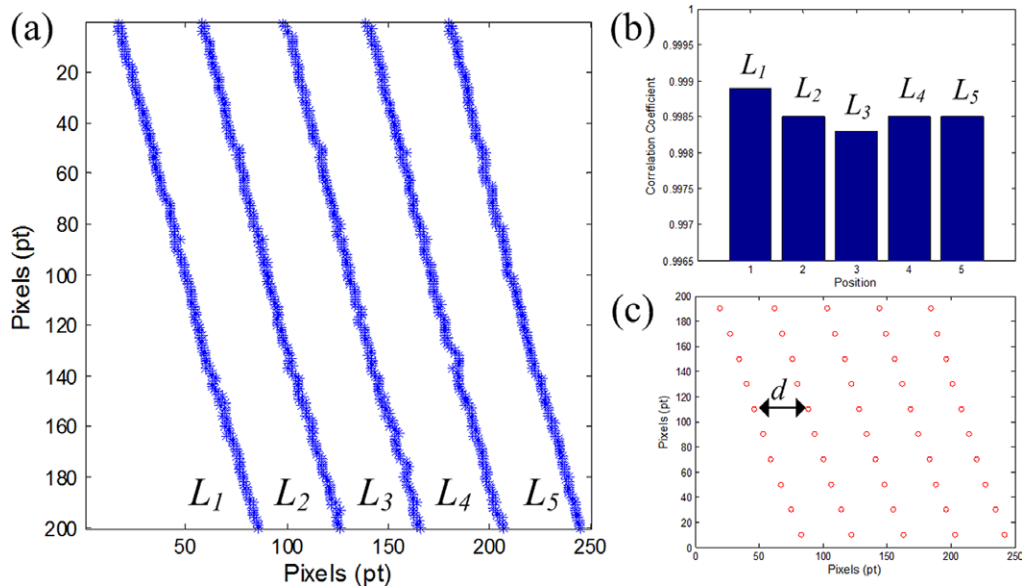


Figure 10. (a) Five edges of the grooves are extracted from the image figure 9(c); (b) shows the correlation coefficient of each edge; and (c) gives ten datasets extracted from (a) to evaluate the groove intervals d .

no data in the pixels of the distortion line, the average value has to be calculated from the data at two nearest points and put in the corresponding pixel. Based on the above method, the distorted data can be corrected line by line.

It is worth noting that 66% of the pixels from the distorted image have a one-to-one relationship with the corrected image for $N = 128$ according to equation (18). The computation of this method is mainly used to process 21% of pixels which are undersampling and 13% of pixels which are oversampling. For example, interpolate for undersampling data and calculate average values for oversampling data. Therefore, if these pixels could be processed with a faster algorithm, the speed of this correction method would be further increased. It will be discussed in our future work.

5. Experimental results and discussions

In order to evaluate the methods mentioned above, during imaging, the original image, the image after the phase-lag

compensation, and the image after nonlinear correction were collected respectively. A piece of the compact disc (CD) with the period of $\sim 1.6\mu\text{m}$ as a test sample was first measured. The images were acquired with 500 points per line (250 points for forward scan and 250 points for backward scan) and 200 lines per frame by using the collection system, and only the forward scanned images were displayed. One image size is thus 250×200 pixels. The phase-lag induced distortion is clearly seen, as shown in figure 9(a). After the phase-lag compensation, the nonlinear distortion can be observed in figure 9(b), where the grooves are narrower at the middle area than those on the two sides. After performing nonlinear distortion correction, the distances between the CD grooves become equally spaced. The final image in figure 9(c) shows that the distortions are effectively eliminated in real-time.

Image linearity was evaluated by extracting five edges of the grooves L_1 – L_5 from figure 9(c) first, as shown in figure 10(a). Then the least-squares fitting method was used for each edge. The linearity was quantified by the correlation coefficients of each edge. By using our home-made program,

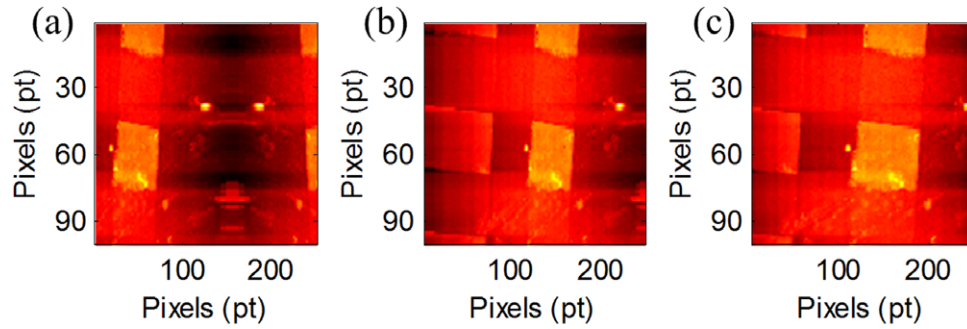


Figure 11. HSAFM scanned images of the TGQ1 grating. (a) The original image; (b) the phase-lag compensation image; and (c) the final image after nonlinear correction. The scan range is $\sim 6\mu\text{m}$ and the imaging rate is at ~ 30 FPS. The movie is shown in the supplementary data as movie2.gif (stacks.iop.org/MST/25/125404).

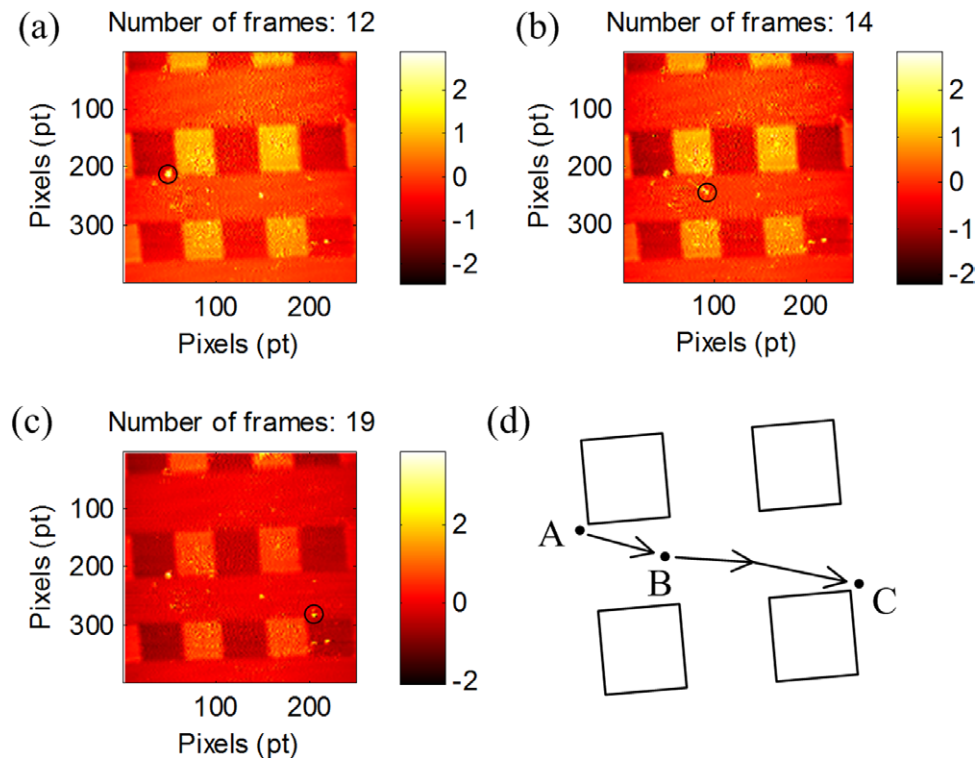


Figure 12. HSAFM images of the TGQ1 grating, showing the motion process of a small particle from the positions (A) to (C) through point (B). (a) The particle at position (A) starts to move. (b) The change of the motion direction of the particle at point (B). (c) The particle finally stops at position (C). (d) The supposed moving path of the particle during its movement. The scan range of the images is $\sim 8\mu\text{m}$ and the imaging rate is ~ 12 FPS. The complete movie is given in the supplementary data as movie3.gif (stacks.iop.org/MST/25/125404).

the minimum value of the correlation coefficients is larger than 0.9986, which shows the good linearity, as given in figure 10(b). In order to verify that groove intervals d in the image are equal, 10 datasets were extracted from figure 10(a), as shown in figure 10(c). The average value of d is 40 pixels and the standard deviation is 1.2 pixels, which also help to illustrate that the image distortions are effectively eliminated.

To further demonstrate the ability of the correction methods, the TGQ1 grating with the period of $3\mu\text{m}$ (NT-MDT Company, Russia) as a calibration sample was then measured. Figure 11(a) is the original image of the sample, from which it is clearly seen that serious image distortion takes place in the middle area of the picture due to the phase-lag. After the phase-lag compensation, the image with only nonlinear distortion is taken, as shown in figure 11(b). As nonlinear correction

continues, the image as given in figure 11(c) shows the distortions are effectively eliminated. The scan range is $\sim 6\mu\text{m}$ and the imaging speed is ~ 30 FPS. It should be mentioned that these images experimentally obtained are in agreement with the simulation results, as given above.

In order to verify the ability for real-time imaging of dynamic processes by using our HSAFM, experiments were performed in such a way that the sample (TGQ1 grating) was moved by manually adjusting the micropositioning stage while imaging. We happened to see an interesting phenomenon, that is, the motion of one of the small dust particles was observed. The particle on the sample surface started to move from its initial position (A) and then slightly changed its moving direction at point (B) and finally stopped at position (C), as shown in figure 12, which shows selected images from the movie captured by HSAFM.

The distance between positions A and C is about $4.8\mu\text{m}$. It is suggested that the particle at position (A) is unstable and it starts to move due to the lateral force of the scanning tip when it impacts on the particle instantaneously. The lateral force acting on the particle is obviously larger than the friction force between the particle and the substrate. It is found that the motion trace of the particle is nonlinear. The change of the motion direction could result from the force between the tip and the particle or between the particle and the substrate, or their combination during its movement. From the nonlinear path of the particle, the rastering tip would be another factor that changes the direction of the particle's motion. During imaging the tip and the particle may collide with each other multiple times. It is believed that the particle at the new position (C) is more stable than that at (A). In fact, it could be difficult to explain the underlying reason for the phenomenon. Nevertheless, these results imply that real-time imaging can be carried out with our HSAFM setup.

6. Conclusion

In conclusion, a resonance-type bimorph-based HSAFM has been developed in our laboratory, which is able to operate in the sample-scan and tip-scan modes. The main characteristic of the resonance-type bimorph-based scanners is the use of a piezoelectric bimorph, where one of the piezo-layers is used to drive the bimorph beam to scan in a high speed and the other is done to sense the bimorph vibration. The sensing signal from the bimorph provides useful information for the correction of the phase-lag induced distortion. Image distortions due to the phase-lag and sinusoidal scanning are analyzed and simulated. A data shift method for compensating the image distortion caused by the phase-lag is presented and nonlinear mapping relations are proposed for correcting the distortion introduced by sinusoidal scanning, respectively. The HSAFM imaging at the maximum rate of ~ 30 frames per second is demonstrated with our data collection and correction program. The image distortions caused by the phase-lag and sinusoidal scanning are effectively eliminated in real-time. This work would provide useful methods for the development of HSAFM and applications in the observation of dynamic processes at nanoscale.

Acknowledgment

This work was supported by the China National Key Basic Research Program 973 (Grant No. 2013CB934004), the National Natural Science Foundation of China (Grant No. 11232013, 11304006), and the Fundamental Research Funds for the Central Universities (Grant No. YWF-13-D2-XX-14).

References

- [1] Ando T 2012 High-speed atomic force microscopy coming of age *Nanotechnology* **23** 062001
- [2] Brown B P, Picco L, Miles M J and Faul C F 2013 Opportunities in high-speed atomic force microscopy *Small* **9** 3201–11
- [3] Ando T, Uchihashi T and Fukuma T 2008 High-speed atomic force microscopy for nano-visualization of dynamic biomolecular processes *Prog. Surf. Sci.* **83** 337–437
- [4] Schitter G and Rost M J 2008 Scanning probe microscopy at video-rate *Mater. Today* **11** 40–8
- [5] Kodera N, Yamamoto D, Ishikawa R and Ando T 2010 Video imaging of walking myosin V by high-speed atomic force microscopy *Nature* **468** 72–6
- [6] Suzuki Y, Sakai N, Yoshida A, Uekusa Y, Yagi A, Imaoka Y, Ito S, Karaki K and Takeyasu K 2013 High-speed atomic force microscopy combined with inverted optical microscopy for studying cellular events *Sci. Rep.* **3** 2131
- [7] Nath R, Chu Y-H, Polomoff N A, Ramesh R and Huey B D 2008 High speed piezoresponse force microscopy: <1 frame per second nanoscale imaging *Appl. Phys. Lett.* **93** 072905
- [8] Huey B D 2007 AFM and acoustics: fast, quantitative nanomechanical mapping *Annu. Rev. Mater. Res.* **37** 351–85
- [9] Iwata F, Ohashi Y, Ishisaki I, Picco L and Ushiki T 2013 Development of nanomanipulator using a high-speed atomic force microscope coupled with a haptic device *Ultramicroscopy* **133** 88–94
- [10] Yan Y, Zou Q and Lin Z 2009 A control approach to high-speed probe-based nanofabrication *Nanotechnology* **20** 175301
- [11] Paul P C, Knoll A W, Holzner F, Despont M and Duerig U 2011 Rapid turnaround scanning probe nanolithography *Nanotechnology* **22** 275306
- [12] Fantner G E, Schitter G, Kindt J H, Ivanov T, Ivanova K, Patel R, Holten-Andersen N, Adams J, Thurner P J and Rangelow I W 2006 Components for high speed atomic force microscopy *Ultramicroscopy* **106** 881–7
- [13] Schitter G, Thurner P J and Hansma P K 2008 Design and input-shaping control of a novel scanner for high-speed atomic force microscopy *Mechatronics* **18** 282–8
- [14] Humphris A, Miles M and Hobbs J 2005 A mechanical microscope: high-speed atomic force microscopy *Appl. Phys. Lett.* **86** 034106
- [15] Hobbs J K, Vasilev C and Humphris A D 2006 VideoAFM—a new tool for high speed surface analysis *Analyst* **131** 251–6
- [16] Picco L, Bozec L, Ulcinas A, Engledew D, Antognozzi M, Horton M and Miles M 2007 Breaking the speed limit with atomic force microscopy *Nanotechnology* **18** 044030
- [17] Seo Y, Choi C, Han S and Han S-J 2008 Real-time atomic force microscopy using mechanical resonator type scanner *Rev. Sci. Instrum.* **79** 103703
- [18] Zhao B, Howard-Knight J, Humphris A, Kailas L, Ratcliffe E, Foster S and Hobbs J 2009 Large scan area high-speed atomic force microscopy using a resonant scanner *Rev. Sci. Instrum.* **80** 093707
- [19] Zhou Y, Shang G, Cai W and Yao J 2010 Cantilevered bimorph-based scanner for high speed atomic force microscopy with large scanning range *Rev. Sci. Instrum.* **81** 053708
- [20] Zhao J, Gong W, Cai W and Shang G 2013 Piezoelectric bimorph-based scanner in the tip-scan mode for high speed atomic force microscope *Rev. Sci. Instrum.* **84** 083706
- [21] Fleming A, Kenton B and Leang K 2010 Bridging the gap between conventional and video-speed scanning probe microscopes *Ultramicroscopy* **110** 1205–14
- [22] Khoury J, Haji-saeed B, Kierstead J, Sengupta S K and Woods C 2007 Spatial demultiplexing/multiplexing approach for image correction and processing for bidirectional resonant scanners *Opt. Eng.* **46** 047001
- [23] Haji-Saeed B, Khoury J, Pyburn D, Sengupta S K, Kierstead J and Woods C L 2007 Mapping approach for image correction and processing for bidirectional resonant scanners *Opt. Eng.* **46** 027007

- [24] Xu L, Tian X, Li X, Shang G and Yao J 2011 Geometric distortion correction for sinusoidally scanned images *Meas. Sci. Technol.* **22** 114023
- [25] Picco L, Dunton P, Ulcinas A, Engledew D, Hoshi O, Ushiki T and Miles M 2008 High-speed AFM of human chromosomes in liquid *Nanotechnology* **19** 384018
- [26] Marinello F, Bariani P, De Chiffre L and Savio E 2007 Fast technique for AFM vertical drift compensation *Meas. Sci. Technol.* **18** 689
- [27] Sarid D 1991 *Scanning Force Microscopy* (New York: Oxford University Press)
- [28] Shang G, Wang C, Wu J, Bai C and Lei F 2001 Shear force scanning near-field optical microscope based on a piezoelectric bimorph cantilever *Rev. Sci. Instrum.* **72** 2344–9
- [29] Lindfors K, Kapulainen M, Ryytty P and Kaivola M 2004 High-sensitivity piezoelectric tube sensor for shear-force detection in scanning near-field optical microscopy *Opt. Laser Technol.* **36** 651–6